

Article

Preparation and Gas-Sensitive Properties of SnO₂@Bi₂O₃ Core-Shell Heterojunction Structure

Jin Liu *, Yixin Gao, Yuanyuan Lv, Mengdi Yang, Haoru Guo, Neng Li, Danyang Bai and Anyi Wang

School of Communication and Information Engineering, Xi'an University of Science and Technology, Xi'an 710054, China

* Correspondence: liujin@xust.edu.cn

Abstract: The SnO₂@Bi₂O₃ core-shell heterojunction structure was designed and synthesized via a hydrothermal method, and the structure and morphology of the synthesized samples were characterized using X-ray diffraction (XRD), scanning electron microscopy (SEM), and X-ray photoelectron spectroscopy (XPS). Based on the conclusions from XRD and SEM, it can be observed that as the hydrothermal temperature increases, the content of Bi₂O₃ coated on the surface of SnO₂ spheres gradually increases, and the diameter of Bi₂O₃ nanoparticles also increases. At a hydrothermal temperature of 160 °C, the SnO₂ spheres are fully coated with Bi₂O₃ nanoparticles. This paper investigated the gas-sensitive performance of the SnO₂@Bi₂O₃ sensor towards ethanol gas. Gas sensitivity tests at the optimal operating temperature of 300 °C showed that the composite prepared at 160 °C achieved a response value of 19.7 for 100 ppm ethanol. Additionally, the composite exhibited excellent response to 100 ppm ethanol, with a response time of only 4 s, as well as good repeatability. The excellent gas-sensitive performance of the SnO₂@Bi₂O₃ core-shell heterojunction towards ethanol gas is attributed to its p-n heterojunction material properties. Its successful preparation contributes to the realization of high-performance heterostructure ethanol gas sensors.

Keywords: SnO₂@Bi₂O₃ heterojunctions; hydrothermal method; gas sensors; ethanol



Academic Editor: Jiaolong Liu

Received: 15 December 2024

Revised: 8 January 2025

Accepted: 9 January 2025

Published: 16 January 2025

Citation: Liu, J.; Gao, Y.; Lv, Y.; Yang, M.; Guo, H.; Li, N.; Bai, D.; Wang, A. Preparation and Gas-Sensitive Properties of SnO₂@Bi₂O₃ Core-Shell Heterojunction Structure. *Nanomaterials* **2025**, *15*, 129. <https://doi.org/10.3390/nano15020129>

Copyright: © 2025 by the authors. Licensee MDPI, Basel, Switzerland. This article is an open access article distributed under the terms and conditions of the Creative Commons Attribution (CC BY) license (<https://creativecommons.org/licenses/by/4.0/>).

1. Introduction

With the rapid development of industry, environmental pollution has become increasingly severe. Large quantities of untreated gasses containing harmful substances are being released into the atmosphere, posing significant threats to human health [1]. As a result, gas detection has become a key area of focus. Gas sensors, which play a vital role in environmental monitoring and air quality detection, have attracted growing research interest. Among them, metal oxide semiconductors (MOS) have garnered significant attention as gas-sensitive materials due to their simple structure, ease of fabrication, and real-time monitoring capabilities [2,3].

Tin dioxide (SnO₂) is a common MOS material and is widely used in gas sensing materials due to its excellent electrical conductivity, wide bandgap ($E_g = 3.6$ eV), tunable resistivity, and sensitivity and selectivity to various gasses [4–6]. However, pure SnO₂ suffers from low response and poor selectivity, and its gas sensing performance has not yet reached the expected targets. Many researchers have employed composite structures to enhance the performance of gas sensors. The formation of heterostructures, composed of two or more semiconductor materials, has been explicitly proven to improve gas sensor performance [7–11]. For instance, SnO₂@SnS₂ heterojunctions exhibited

excellent performance in NO₂ detection [12]. Researchers synthesized NiO/SnO₂ hollow spheres and constructed p-n heterojunctions, significantly enhancing the sensitivity to triethylamine [13]. J.H. Kim et al. demonstrated that Co₃O₄/SnO₂ composite nanofibers exhibited significantly enhanced response to acetone gas at 350 °C compared to pure SnO₂ [14]. Zhang et al. developed a novel gas sensor based on ZnO/SnO₂, which showed a response to 2000 ppm ethanol vapor that was 7 times higher than that of the original ZnO sensor [15]. Furthermore, Chen et al. reported that the SnO₂/TiO₂ heterojunction sensor achieved a response value of 9.58 to 100 ppm ethanol, which was 1.88 times that of SnO₂ nanoparticles [16]. This improvement is attributed to the synergistic effect of band structure modulation and the formation of heterojunctions between the two semiconductors, which increases the electron depletion layer and improves charge carrier separation.

Bismuth oxide (Bi₂O₃) is another common MOS material with a bandgap of 2.79 eV. Due to its high refractive index and high dielectric constant, it has promising application prospects [17]. It is often combined with other metal oxides for constructing gas sensors [18–21]. For example, A. Montenegro et al. synthesized SnO₂-Bi₂O₃ composites via the polymer precursor method, demonstrating that the introduction of bismuth significantly enhanced the sensor's response to oxygen [22]. Jae Hoon Bang et al. proposed a highly sensitive and selective NO₂ sensor based on Bi₂O₃-modified branched SnO₂ nanowires (NWs) [23]. Additionally, Yang et al. incorporated Bi₂O₃ particles as external additives onto the surface of SnO₂ nanoparticles (NPs) for the efficient detection of oxygenated volatile organic compounds (VOCs) [24]. Therefore, SnO₂@Bi₂O₃ composite materials exhibit potential for achieving reliable gas sensors, warranting further investigation in this field.

In this paper, SnO₂@Bi₂O₃ core-shell heterojunctions were prepared at different temperatures using a hydrothermal method. The crystal structure, microstructure, and chemical states of the materials were characterized. The gas-sensing performance was tested to determine the optimal operating temperature of the sensor. The response and recovery times of the sensor were calculated, and the transient current curves of the sensors exposed to 5–100 ppm ethanol were analyzed. The effect of sensor repeatability was explored. This paper focuses on analyzing the gas-sensing mechanism of the sensors and reveals that the improvement in ethanol gas-sensing performance of SnO₂@Bi₂O₃ composites primarily originates from the p-n heterojunction.

2. Experimental Section

2.1. Synthesis of SnO₂

First, 8.098 g of SnCl₄·5H₂O (Beijing Tianyun Chemical Reagent Co., Ltd., Beijing, China) and 0.2 g of PVP (polyvinylpyrrolidone) (Sinopharm Chemical Reagent Co., Ltd., Shanghai, China) were dissolved in 35 mL of deionized water and stirred for 30 min until fully mixed. Subsequently, 6.02 g of NaOH (Sichuan Xilong Science Co., Ltd., Chengdu, China) was dissolved in 35 mL of deionized water and stirred at room temperature for 30 min to form a colorless and transparent NaOH solution. The NaOH solution was added dropwise to the SnCl₄·5H₂O solution, and the mixture was stirred for 30 min to form a transparent and uniform precursor solution. The precursor solution was transferred into a polytetrafluoroethylene reactor and reacted at 180 °C for 10 h. After natural cooling to room temperature, the sample was collected and washed five times with deionized water and anhydrous ethanol until neutral. Finally, the sample was dried at 60 °C for 12 h to obtain the final SnO₂ sample.

2.2. Synthesis of SnO₂@Bi₂O₃

First, 0.679 g of Bi(NO₃)₃·5H₂O (Sinopharm Chemical Reagent Co., Ltd., Shanghai, China) and 0.168 g of NaOH were dissolved separately in 35 mL of deionized water and

stirred for 30 min to form uniform solutions. The NaOH solution was added dropwise to the $\text{Bi}(\text{NO}_3)_3 \cdot 5\text{H}_2\text{O}$ solution, forming a stable solution. Subsequently, 0.8 g of SnO_2 prepared in the first step was added, and the mixture was stirred for another 30 min. The resulting solution was transferred into a polytetrafluoroethylene reactor and reacted at different temperatures (100 °C, 120 °C, 140 °C, and 160 °C) for 4 h. After natural cooling to room temperature, the samples were collected and washed five times with deionized water and anhydrous ethanol until neutral. Finally, the sample was dried at 70 °C for 12 h to obtain the final samples.

2.3. Material Characterization

The crystal structure of the samples was measured using an X-ray diffractometer (XRD, Bruker D8 Advance, Bruker Corporation, Karlsruhe, Germany). The microscopic morphology and element content of the prepared samples were analyzed using a scanning electron microscope (SEM, GeminiSEM 360, Carl Zeiss AG, Oberkochen, Germany) with energy-dispersive X-ray spectrum (EDS). X-ray photoelectron spectroscopy (XPS, Thermo Scientific-ESCALAB Xi+, Thermo Fisher Scientific, Waltham, MA, USA) was used to determine the surface composition and chemical states of the elements.

2.4. Sensor Fabrication and Gas Sensing

The fabrication process of the gas sensor is as follows: the prepared sample was mixed with an appropriate amount of deionized water and grinded to form a slurry. The slurry was then coated onto a clean ceramic tube equipped with a pair of gold electrodes to serve as the testing electrode. The ceramic tube was sintered in air at 300 °C for 3 h to enhance the material's stability. Finally, a nickel–chromium heating wire was inserted and welded onto the hexagonal base of the ceramic tube, forming an indirectly heated gas sensor.

The sensor response was defined as I_g/I_a , where I_a represents the sensor current in air and I_g represents the current in the target gas.

3. Results and Discussion

3.1. Characterization of the $\text{SnO}_2@Bi_2O_3$

The crystal structures of SnO_2 , $\text{SnO}_2@Bi_2O_3$ (100 °C), $\text{SnO}_2@Bi_2O_3$ (120 °C), $\text{SnO}_2@Bi_2O_3$ (140 °C), and $\text{SnO}_2@Bi_2O_3$ (160 °C) samples were analyzed by XRD, and the results are presented in Figure 1. As shown in the figure, the XRD peaks of the synthesized SnO_2 powder were observed at $2\theta = 26.709^\circ$, 34.294° , 37.911° , and 52.03° , corresponding to the (110), (101), (200), and (211) planes of the tetragonal phase SnO_2 (JCPDS No. 41-1445). This indicates that the SnO_2 synthesized by the hydrothermal method possesses high purity and good crystallinity. For the $\text{SnO}_2@Bi_2O_3$ composite material, the diffraction peaks not only include those of tetragonal SnO_2 but also exhibit additional peaks at $2\theta = 27.526^\circ$, 33.419° , and 46.474° , which correspond to the (120), (200), and (122) planes of Bi_2O_3 (JCPDS No. 41-1449). This confirms that the prepared material is indeed $\text{SnO}_2@Bi_2O_3$. Moreover, the intensity of the Bi_2O_3 diffraction peaks increased with the reaction temperature, indicating improved crystallinity or higher Bi_2O_3 content in the $\text{SnO}_2@Bi_2O_3$ composite.

The morphology and microstructure of the $\text{SnO}_2@Bi_2O_3$ composite materials were further investigated using SEM. As shown in Figure 2a, pure SnO_2 exhibits a typical spherical structure with a rough surface and an average diameter of approximately 4 μm . Figure 2b shows the $\text{SnO}_2@Bi_2O_3$ composite synthesized at 100 °C, where a small amount of Bi_2O_3 is sparsely distributed on the SnO_2 surface. This could be attributed to the fact that at low temperatures, the Bi_2O_3 grains are relatively small and not fully crystallized, existing predominantly in an amorphous or poorly crystallized state. As the temperature increased to 120 °C, Bi_2O_3 gradually formed sheet-like and flocculent structures, partially

covering the SnO₂ surface (Figure 2c). The increase in temperature promotes further crystallization of Bi₂O₃ and may lead to the formation of two-dimensional structures, such as sheet-like shapes, through self-assembly. The formation of these sheet-like structures can be attributed to the differences in crystal surface energy and growth rates, causing Bi₂O₃ to preferentially grow along specific crystal planes, resulting in sheet-like or flocculent morphologies. When the temperature was further elevated to 140 °C (Figure 2d), the morphology of Bi₂O₃ underwent a significant change, with the sheet-like and flocculent structures disappearing and being replaced by well-defined polyhedral structures. The SnO₂ surface was almost completely covered by Bi₂O₃, with the coverage becoming more uniform, though some residual sheet-like structures remained. At 160 °C (Figure 2e), the sheet-like Bi₂O₃ structures completely disappeared, and the surface morphology transformed into uniform polyhedron, resulting in a fully encapsulated structure, consistent with the XRD results. This transformation may be related to the rearrangement of crystals, crystal plane growth, and self-assembly mechanisms at high temperatures. At elevated temperatures, the solubility and diffusion rate of Bi₂O₃ increase, facilitating the crystal growth and optimized arrangement of Bi₂O₃ grains, driving the transition from sheet-like structures to polyhedral morphologies. The interfacial interaction between the SnO₂ surface and Bi₂O₃ also promotes the uniform coating of Bi₂O₃, thereby forming stable polyhedral nanoparticles.

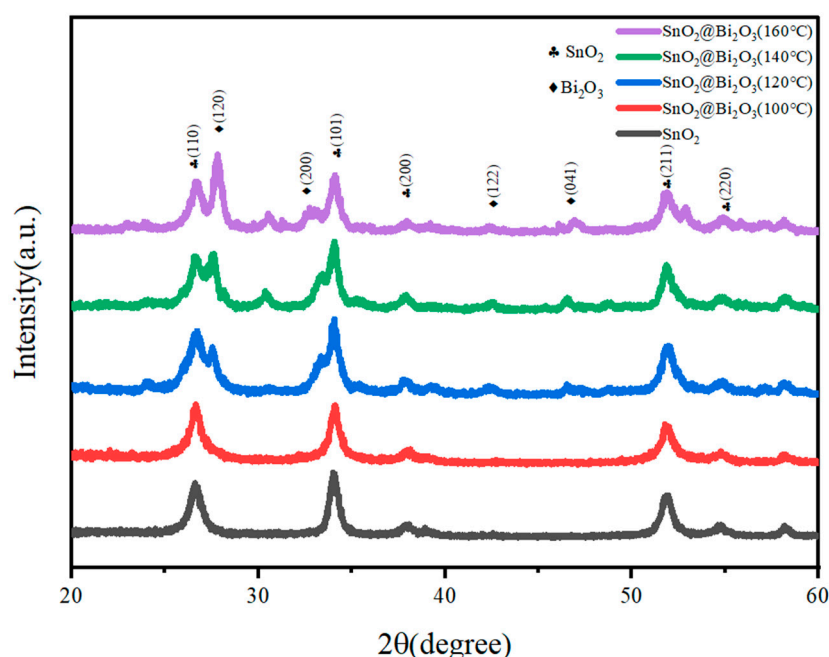


Figure 1. XRD spectra of SnO₂, SnO₂@Bi₂O₃ (100 °C), SnO₂@Bi₂O₃ (120 °C), SnO₂@Bi₂O₃ (140 °C), and SnO₂@Bi₂O₃ (160 °C).

EDS mapping of the SnO₂@Bi₂O₃ sample prepared at 160 °C was performed to determine the distribution and content of elements on the sample surface. As shown in Figure 3b–d, oxygen (O, yellow), tin (Sn, red), and bismuth (Bi, green) are uniformly distributed across the sample surface. Further quantitative analysis of the elemental composition (Figure 3e and Table 1) revealed that the sample contains 79.3% O, 14.6% Bi, and 6.1% Sn. Additionally, no other elements were detected, indicating that the prepared sample is composed of SnO₂@Bi₂O₃ composite material, which is consistent with the results of XRD and SEM analyses.

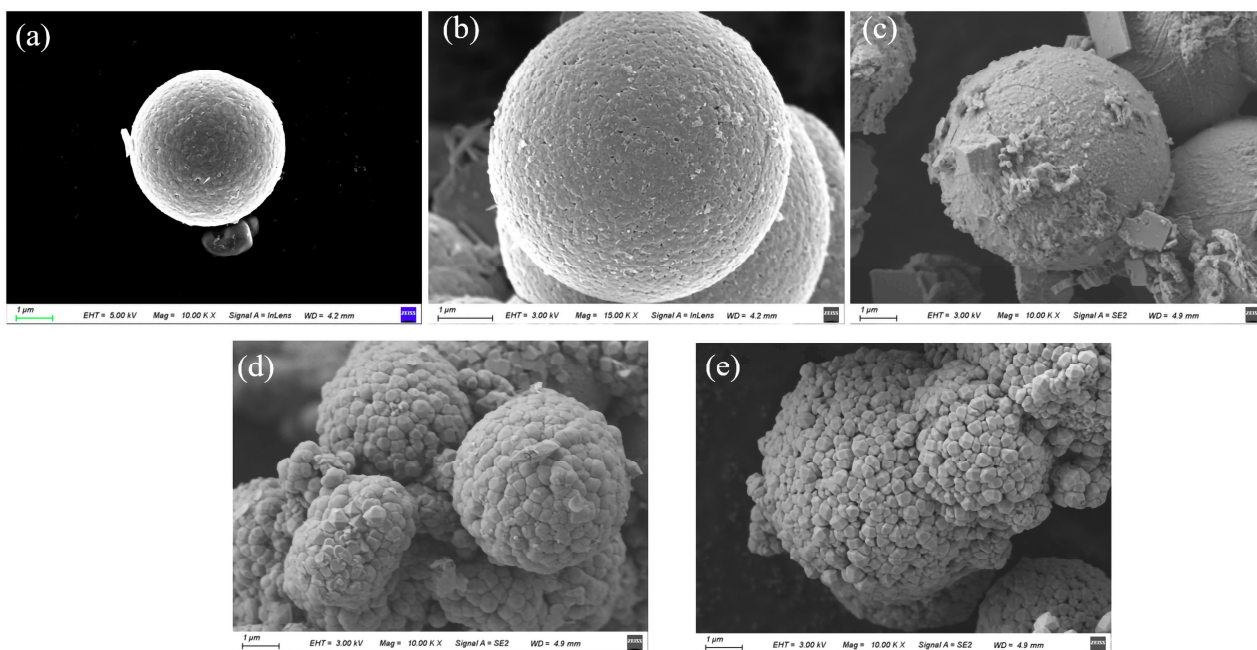


Figure 2. SEM images of (a) SnO₂, (b) SnO₂@Bi₂O₃ (100 °C), (c) SnO₂@Bi₂O₃ (120 °C), (d) SnO₂@Bi₂O₃ (140 °C), and (e) SnO₂@Bi₂O₃ (160 °C).

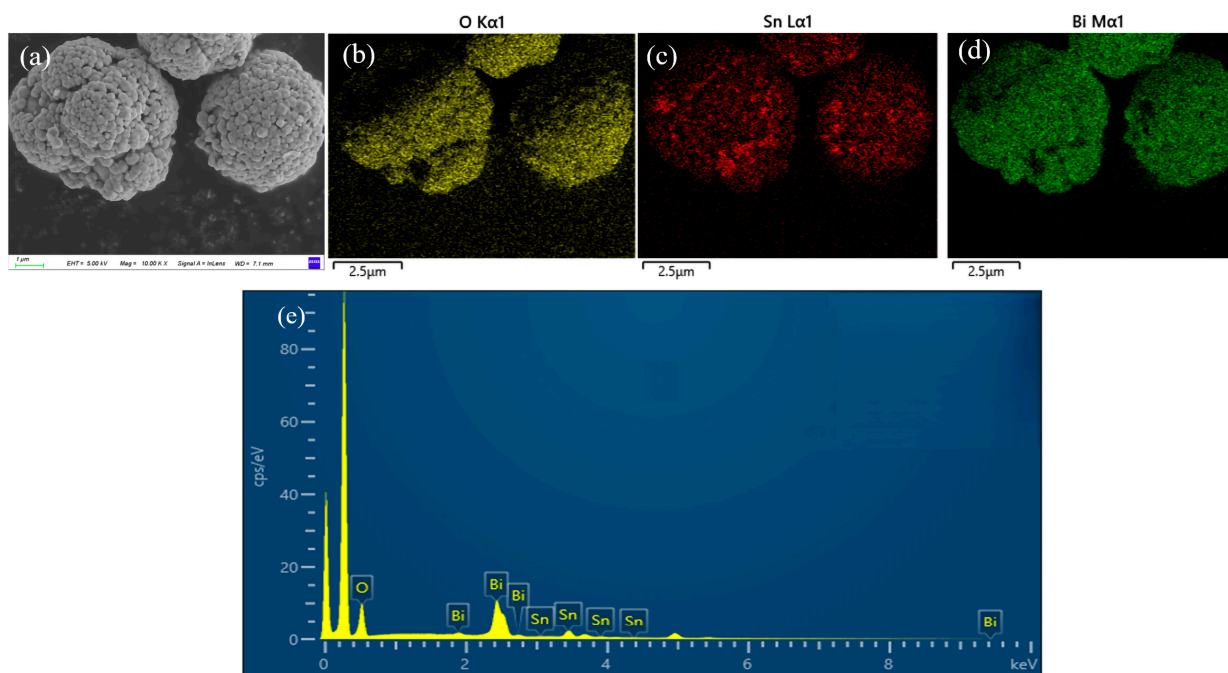


Figure 3. (a) SEM image of SnO₂@Bi₂O₃ (160 °C); (b–d) Elemental mapping images of O, Sn, and Bi, respectively; (e) EDS of SnO₂@Bi₂O₃ (160 °C).

Table 1. Elemental composition of the SnO₂@Bi₂O₃ (160 °C) sample.

Element	Atomic %
O	79.3
Sn	6.1
Bi	14.6
Total	100

The structure and specific surface area of materials are key factors affecting their gas sensitivity performance. Increasing the contact area between gas-sensitive materials and gases can enhance the oxygen adsorption capacity on the material surface. In this study, both the SnO₂@Bi₂O₃ (160 °C) composite material and pure SnO₂ were tested using BET and BJH methods. As shown in Figure 4a, the adsorption–desorption isotherms of the SnO₂@Bi₂O₃ (160 °C) composite material can be classified as Type IV, while those of SnO₂ can be classified as Type II. Figure 4b shows the pore size distribution curves for both SnO₂@Bi₂O₃ (160 °C) and pure SnO₂, with the main peaks occurring at 2–4 nm. Table 2 presents the BET data for both SnO₂@Bi₂O₃ (160 °C) and SnO₂, where the specific surface area of SnO₂@Bi₂O₃ (160 °C) is 31.2148 m²/g, approximately 5 times that of the pure SnO₂ nanospheres (6.7419 m²/g). This indicates that the SnO₂@Bi₂O₃ composite material prepared in this study has a larger specific surface area, enhancing the rate of electron exchange between ethanol gas and the semiconductor material, thus creating favorable conditions for the adsorption, diffusion, and reaction of the test gas. The average pore diameter of SnO₂@Bi₂O₃ (160 °C) is about 2.9790 nm, slightly larger than that of SnO₂ at 2.8669 nm. The pore volume of SnO₂@Bi₂O₃ (160 °C) is 0.020202 cm³/g, significantly greater than that of SnO₂ at 0.004116 cm³/g, corresponding to its higher specific surface area, suggesting that the material provides more pore space for gas adsorption.

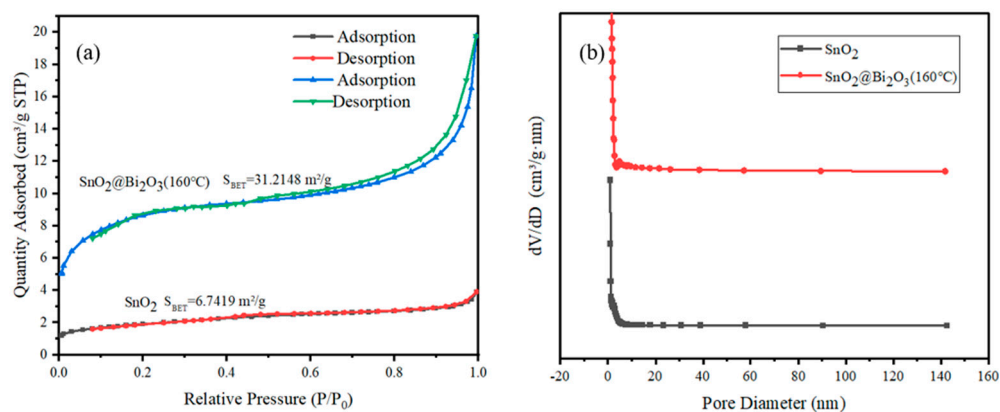


Figure 4. Nitrogen adsorption–desorption isotherms (a) and pore size distribution curves (b) for pure SnO₂ and SnO₂@Bi₂O₃ (160 °C).

Table 2. The BET specific surface areas of different samples.

Samples	S _{BET} (m ² /g)	Average Pore Diameter (nm)	Pore Volume (cm ³ /g)
SnO ₂	6.7419	2.8669	0.004116
SnO ₂ @Bi ₂ O ₃ (160 °C)	31.2148	2.9790	0.020202

The chemical states and surface composition of the SnO₂@Bi₂O₃ composite prepared at 160 °C were analyzed using XPS, as shown in Figure 5. The survey spectrum (Figure 5a) reveals distinct peaks corresponding to Sn, O, and Bi elements, confirming their presence in the sample. The signal from C is attributed to calibration, with the C 1s peak at 284.8 eV used as the reference for calibration. Figure 5b shows the high-resolution Bi 4f spectrum, with peaks at binding energies of 159.35 eV and 164.65 eV, corresponding to Bi 4f_{7/2} and Bi 4f_{5/2}, respectively, which are characteristic peaks of Bi³⁺ [25,26]. The high-resolution Sn 3d spectrum (Figure 5c) exhibits peaks at 487.15 eV and 495.55 eV, corresponding to Sn 3d_{5/2} and Sn 3d_{3/2}, indicating that Sn exists in the form of Sn⁴⁺ in the composite [27,28]. Figure 5d presents the high-resolution O 1s spectrum, which can be divided into three sub-peaks with binding energies at 529.44 eV, 530.08 eV, and 531.45 eV, corresponding to oxygen

in Bi_2O_3 (blue), oxygen in SnO_2 (green), and adsorbed oxygen (purple), respectively [29,30]. The XPS results further confirm that the $\text{SnO}_2@/\text{Bi}_2\text{O}_3$ composite consists of SnO_2 and Bi_2O_3 .

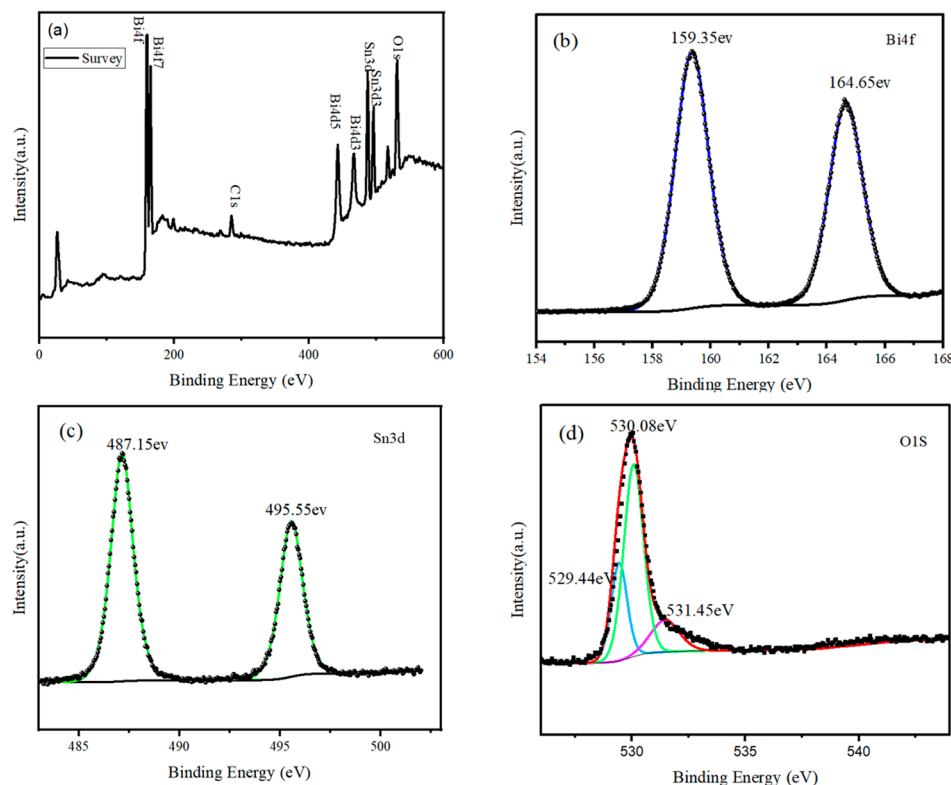


Figure 5. XPS spectra of $\text{SnO}_2@/\text{Bi}_2\text{O}_3$ (160 °C): (a) Survey spectrum, (b) Bi 4f spectrum, (c) Sn 3d spectrum, and (d) O 1s spectrum.

3.2. Gas-Sensing Performances

Metal oxide semiconductors require sufficient operating temperatures to activate the surface adsorption of oxygen and promote chemical reactions. Thus, the optimum operating temperature needs to be determined [31–33]. As shown in Figure 6a, the response of the $\text{SnO}_2@/\text{Bi}_2\text{O}_3$ sensor prepared at 160 °C to 100 ppm ethanol was tested over a temperature range of 50 °C to 300 °C. The response value increased with rising temperature and reached a maximum of 19.7 at 300 °C. This indicates that the optimum operating temperature of the $\text{SnO}_2@/\text{Bi}_2\text{O}_3$ (160 °C) sensor is 300 °C. High selectivity is a critical requirement for gas sensors to avoid interference from other gasses during the detection process. Thus, the selectivity of the $\text{SnO}_2@/\text{Bi}_2\text{O}_3$ (160 °C) sensor was tested at 300 °C against various gasses (including NO_2 , NH_3 , toluene, H_2 , and CO) at a concentration of 100 ppm, as shown in Figure 6b. The response values for NO_2 , CO, NH_3 , toluene, and H_2 were 12.09, 12.9, 13.47, 16.63, and 11.08, respectively, which were all lower than the response value of 19.7 for ethanol. This demonstrates the excellent selectivity of the $\text{SnO}_2@/\text{Bi}_2\text{O}_3$ (160 °C) sensor. At the optimal operating temperature of 300 °C, the responses of SnO_2 and $\text{SnO}_2@/\text{Bi}_2\text{O}_3$ composites prepared at different temperatures to 100 ppm ethanol gas were compared, as shown in Figure 6c. It can be observed that SnO_2 exhibits the lowest response value, while $\text{SnO}_2@/\text{Bi}_2\text{O}_3$ (160 °C) shows the highest response value. According to Table 3, it is evident that the response value of SnO_2 is approximately 9, whereas the response values of $\text{SnO}_2@/\text{Bi}_2\text{O}_3$ (100 °C), $\text{SnO}_2@/\text{Bi}_2\text{O}_3$ (120 °C), and $\text{SnO}_2@/\text{Bi}_2\text{O}_3$ (140 °C) were 9, 10.5, and 13.6, respectively. The highest response value of 19.7 was observed for $\text{SnO}_2@/\text{Bi}_2\text{O}_3$ (160 °C), significantly outperforming the other samples.

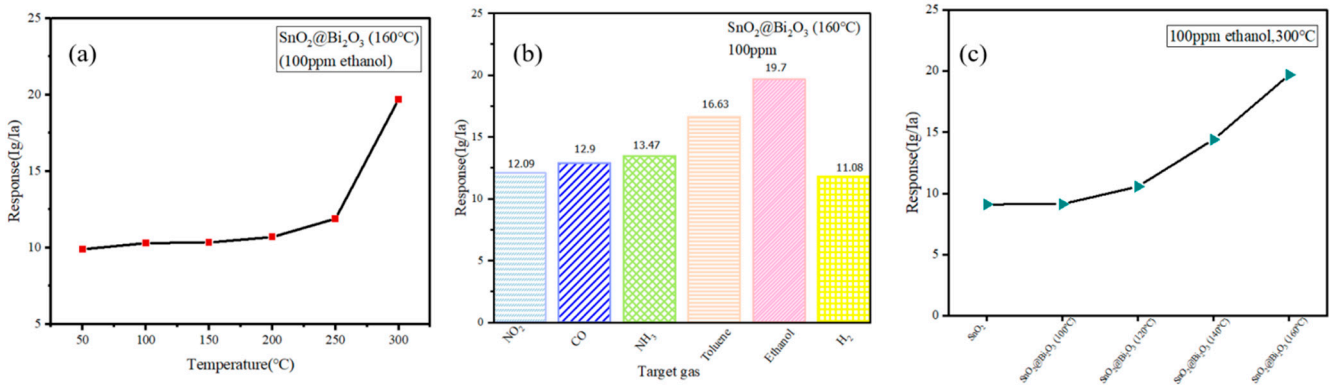


Figure 6. (a) Response of SnO₂@Bi₂O₃ (160 °C) to 100 ppm ethanol at different operating temperatures; (b) Selectivity of SnO₂@Bi₂O₃ (160 °C) at 300 °C for various gasses; (c) Response of SnO₂, SnO₂@Bi₂O₃ (100 °C), SnO₂@Bi₂O₃ (120 °C), SnO₂@Bi₂O₃ (140 °C), and SnO₂@Bi₂O₃ (160 °C) to 100 ppm ethanol at 300 °C.

Table 3. Response of SnO₂, SnO₂@Bi₂O₃ prepared at different temperatures to 100 ppm ethanol at 300 °C.

Ethanol Gas (100 ppm)	Sensor Response
SnO ₂	9
SnO ₂ @Bi ₂ O ₃ (100 °C)	9
SnO ₂ @Bi ₂ O ₃ (120 °C)	10.5
SnO ₂ @Bi ₂ O ₃ (140 °C)	13.6
SnO ₂ @Bi ₂ O ₃ (160 °C)	19.7

As shown in Figure 7a, the transient current curves of the SnO₂@Bi₂O₃ sensor prepared at 160 °C to ethanol gas at 300 °C indicate gas concentrations ranging from 5 ppm to 100 ppm. It can be observed from the figure that as the ethanol gas concentration increases, the current of the SnO₂@Bi₂O₃ (160 °C) sensor shows a continuous upward trend, reaching a maximum value of approximately 32 nA at 100 ppm ethanol gas. The response and recovery characteristics of the SnO₂@Bi₂O₃ (160 °C) sensor to 100 ppm ethanol at 300 °C are shown in Figure 7b. The response and recovery times were 4 s and 11 s, respectively, demonstrating the sensor’s fast response and recovery capabilities. Figure 7c presents the transient current curves of the SnO₂@Bi₂O₃ (160 °C) sensor over ten cycles for 100 ppm ethanol at 300 °C. The analysis indicates that the current of the SnO₂@Bi₂O₃ (160 °C) sensor remained stable over time, with negligible fluctuations, consistently maintaining a value of approximately 32 nA. This result demonstrates the excellent repeatability of the sensor.

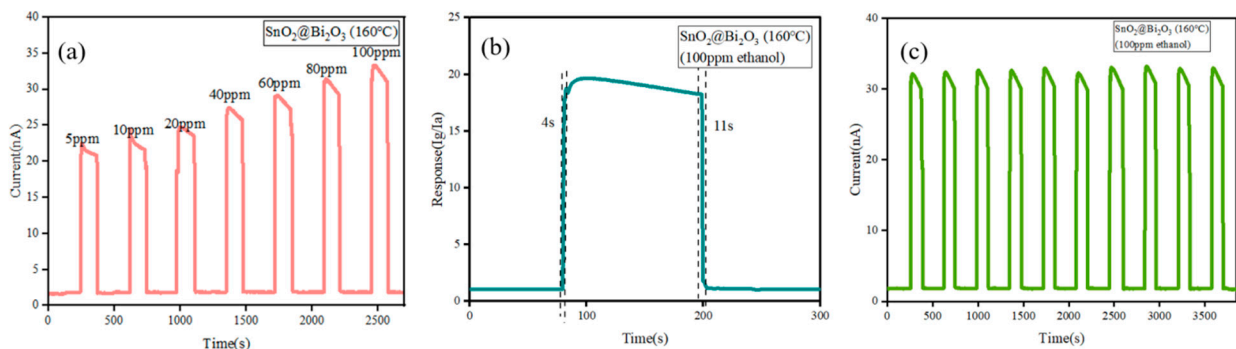


Figure 7. (a) Transient current curves of the SnO₂@Bi₂O₃ (160 °C) sensor to different concentrations of ethanol at 300 °C; (b) Response and recovery curves of the SnO₂@Bi₂O₃ (160 °C) sensor to 100 ppm ethanol at 300 °C; (c) Transient current curves of the SnO₂@Bi₂O₃ (160 °C) sensor over ten cycles for 100 ppm ethanol at 300 °C.

Figure 8a shows the response of the $\text{SnO}_2@\text{Bi}_2\text{O}_3$ (160 °C) sensor to the target gas (ethanol) and interfering gasses (NO_2 , NH_3 , toluene, H_2 , and CO) at a concentration of 5 ppm. The decision to test these gasses at low concentrations is based on the fact that ethanol is typically derived from chemical production, while other gasses (NO_2 , NH_3 , toluene, H_2 , and CO) are often produced by industrial emissions. These gasses may coexist in the environment, and ethanol leaks in the environment generally occur at low concentrations. However, when mixed with other gasses, the accuracy of detection could be affected. Therefore, the sensor's response to these gasses was tested at a low concentration of 5 ppm.

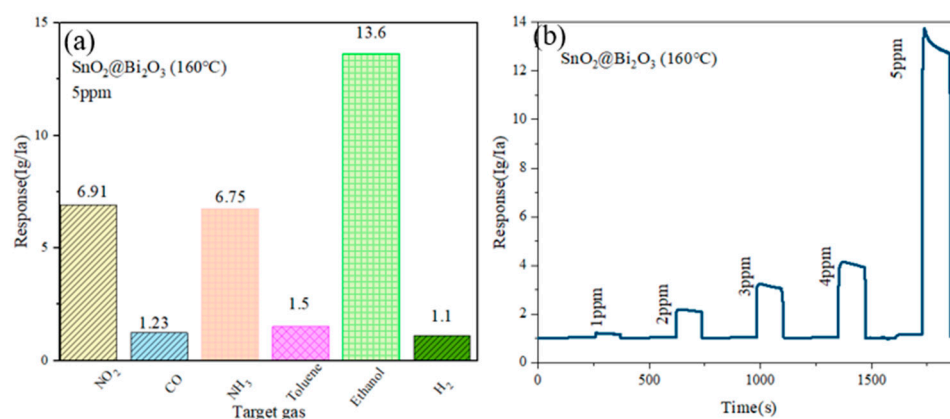


Figure 8. (a) $\text{SnO}_2@\text{Bi}_2\text{O}_3$ (160 °C) sensor response to 5 ppm of different gasses; (b) Response of $\text{SnO}_2@\text{Bi}_2\text{O}_3$ (160 °C) to 1–5 ppm concentration of ethanol.

At 300 °C, the $\text{SnO}_2@\text{Bi}_2\text{O}_3$ (160 °C) sensor showed a response value of 13.6 to 5 ppm ethanol gas, while its response values to other interfering gasses (NO_2 , NH_3 , toluene, H_2 , and CO) at the same concentration were 6.91, 6.75, 1.5, 1.1, and 1.23, respectively. It can be observed that the sensor's response to the target gas ethanol is significantly higher than its response to the interfering gasses. This indicates that even under low concentration conditions, the $\text{SnO}_2@\text{Bi}_2\text{O}_3$ (160 °C) sensor can effectively detect ethanol gas. Figure 8b shows the test results of the $\text{SnO}_2@\text{Bi}_2\text{O}_3$ (160 °C) sensor within the ethanol concentration range of 1–5 ppm. It can be observed that the sensor has no response below 1 ppm, but begins to respond at 1 ppm, with a response value of 1.21, indicating a detection limit of 1 ppm. According to Table 4, the response values remain stable at approximately 1.21 in the range of 1 ppm to 1.4 ppm but increase significantly to 1.562 at 1.5 ppm, demonstrating a resolution of 0.5 ppm for the $\text{SnO}_2@\text{Bi}_2\text{O}_3$ (160 °C) sensor.

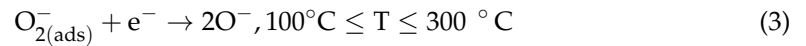
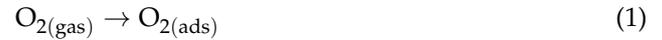
Table 4. Response of $\text{SnO}_2@\text{Bi}_2\text{O}_3$ (160 °C) sensor to different concentrations of ethanol gas.

Concentration of Ethanol (ppm)	Sensor Response
1	1.21
1.1	1.21
1.2	1.21
1.3	1.21
1.4	1.21
1.5	1.562

3.3. Gas Sensing Mechanism

SnO_2 is a typical n-type semiconductor metal oxide that follows the gas sensing mechanism of n-type semiconductors. The adsorption and desorption of target gas molecules on the surface of SnO_2 cause changes in its resistance [34]. When the SnO_2 sensor is exposed to air at its optimal operating temperature, a large amount of oxygen is adsorbed onto the

material's surface. At this point, some conduction band electrons transfer to the adsorbed oxygen, existing in the form of O^- , forming a thick depletion layer [35–38]. As a result, the potential barrier is higher, the resistance increases, and the current decreases. The specific reaction process is as follows:



When the SnO_2 sensor comes into contact with ethanol ($\text{C}_2\text{H}_5\text{OH}$) gas, the adsorbed oxygen on the surface reacts with $\text{C}_2\text{H}_5\text{OH}$ to produce CO_2 and H_2O , as shown in Figure 9a. In this process, electrons return to the conduction band of the sensing material, thinning the depletion layer, thereby reducing the sensor's resistance and increasing the current. The reaction equation is as follows:

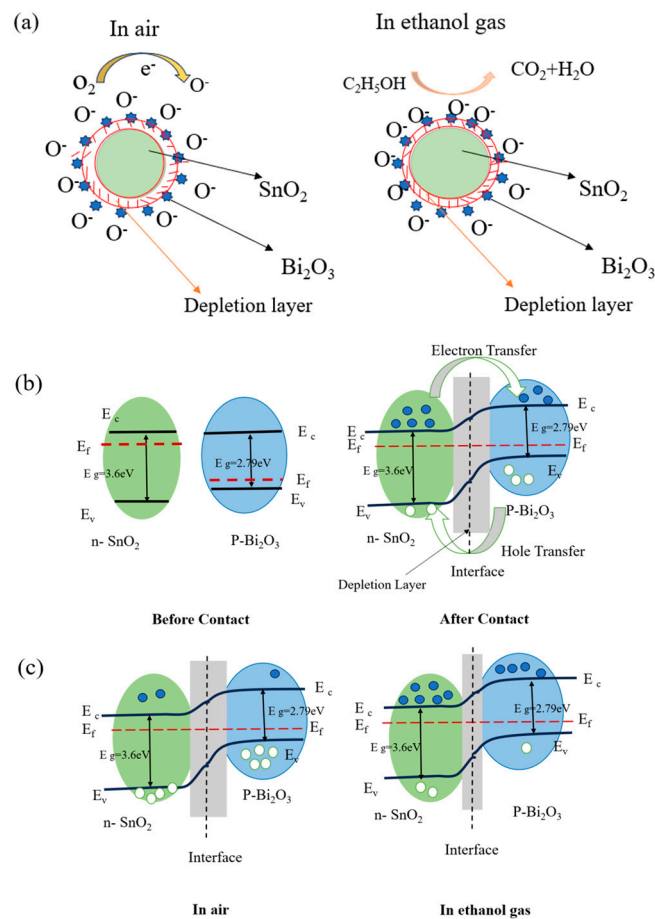
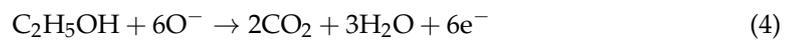


Figure 9. (a) Schematic diagram of the sensing mechanism of the $\text{SnO}_2@Bi_2O_3$ core-shell heterojunction when exposed to air and ethanol; (b) Band diagrams of SnO_2 and Bi_2O_3 before and after contact; (c) Band diagram of the $\text{SnO}_2@Bi_2O_3$ core-shell heterojunction in air and ethanol gas.

When the sensor is returned to normal air from the tested gas, oxygen re-adsorbs onto the surface of SnO_2 , and the conduction band electrons exist again in the form of O^- , causing the resistance to increase and the current to decrease.

The enhanced sensitivity of the $\text{SnO}_2@Bi_2O_3$ composite material to ethanol gas may be attributed to the heterojunction effect [39–41]. Based on the grain boundary potential barrier model, Figure 9b shows that SnO_2 and Bi_2O_3 materials have different Fermi energy levels.

When SnO₂ is combined with Bi₂O₃ to form an n-p heterojunction, electrons flow from the Fermi level of SnO₂ (which is higher) to the Fermi level of Bi₂O₃ (which is lower) until a dynamic equilibrium is reached. At this point, the energy bands of SnO₂ and Bi₂O₃ bend in the space charge region of the n-p junction, forming a potential barrier. Figure 9c illustrates that when the SnO₂@Bi₂O₃ heterostructure is exposed to reducing ethanol gas, ethanol reacts with the oxygen adsorbed (O⁻) on the surface of SnO₂, releasing a large number of electrons. These electrons are injected into the conduction band of SnO₂, lowering its resistance. Simultaneously, some electrons diffuse to the p-type Bi₂O₃ interface, causing electron-hole recombination and reducing the hole concentration in Bi₂O₃, which further decreases the thickness of the depletion layer and the height of the interface potential barrier. Moreover, ethanol gas may also directly react with the holes on the surface of Bi₂O₃, releasing more electrons. These electrons are transferred to the conduction band of SnO₂, further reducing the overall resistance of the composite material and increasing the current. Ultimately, the synergistic effects of these processes significantly enhance the sensitivity of the SnO₂@Bi₂O₃ heterojunction material to ethanol gas [42–45].

4. Conclusions

In summary, this study successfully prepared SnO₂@Bi₂O₃ heterostructures via a simple hydrothermal method and evaluated their gas-sensing performance. As the hydrothermal temperature increases, the content of Bi₂O₃ coated on the surface of SnO₂ spheres gradually increases, and the diameter of the Bi₂O₃ nanoparticles also increases. When the hydrothermal temperature reaches 160 °C, the SnO₂ spheres are completely coated with Bi₂O₃ nanoparticles. The test results demonstrated that the SnO₂@Bi₂O₃ heterostructure exhibited excellent sensitivity to ethanol gas. At 300 °C, the response value of SnO₂@Bi₂O₃ (160 °C) to 100 ppm ethanol reached 19.7, with response and recovery times of 4 s and 11 s, respectively. The composite material also showed excellent repeatability. Based on the characterization results, the performance enhancement was attributed to the presence of p-n heterojunctions on the material surface. Therefore, the SnO₂@Bi₂O₃ heterostructure provides a promising strategy for ethanol gas detection and sensor development.

Author Contributions: Conceptualization, J.L. and Y.G.; formal analysis, J.L. and Y.L.; investigation, Y.G. and J.L.; writing—original draft preparation, Y.G.; writing—review and editing, Y.G., Y.L. and M.Y.; visualization, H.G., N.L. and D.B.; supervision, A.W.; projection administration, J.L. and Y.L.; funding acquisition, J.L. and Y.L. All authors have read and agreed to the published version of the manuscript.

Funding: This research was funded by National Natural Youth Science Foundation of China (Grant number: 62205269), Education Department of Shaanxi Province Natural Special Project (Grant number: 22JK0467), Xi'an Beilin District Science and Technology Project (Grant number: GX2230), Natural Science Basic Research Plan in Shaanxi Province of China (Grant number: 2023-JC-YB-595), Science and Technology Program of Xi'an, China (Grant number: 24GXF0048).

Data Availability Statement: The data provided in this study are available from the corresponding author.

Conflicts of Interest: The authors declare no conflicts of interest.

References

1. Reddy, P.A.K.; Reddy, P.V.L.; Kwon, E.; Kim, K.-H.; Akter, T.; Kalagara, S. Recent advances in photocatalytic treatment of pollutants in aqueous media. *Environ. Int.* **2016**, *91*, 94–103. [[CrossRef](#)]
2. Krishna, K.G.; Parne, S.; Pothukanuri, N.; Kathirvelu, V.; Gandhi, S.; Joshi, D. Nanostructured metal oxide semiconductor-based gas sensors: A comprehensive review. *Sens. Actuators A* **2022**, *341*, 113578. [[CrossRef](#)]

3. Pasupuleti, K.S.; Reddeppa, M.; Chougule, S.S.; Bak, N.-H.; Nam, D.-J.; Jung, N.; Cho, H.D.; Kim, S.-G.; Kim, M.-D. High performance langasite based SAW NO₂ gas sensor using 2D g-C₃N₄@TiO₂ hybrid nanocomposite. *J. Hazard. Mater.* **2022**, *427*, 128174. [[CrossRef](#)] [[PubMed](#)]
4. Meng, X.; Bi, M.; Xiao, Q.; Gao, W. Ultrasensitive gas sensor based on Pd/SnS₂/SnO₂ nanocomposites for rapid detection of H₂. *Sens. Actuators B* **2022**, *359*, 131612. [[CrossRef](#)]
5. Yu, H.M.; Li, J.Z.; Luo, W.B.; Li, Z.Y.; Tian, Y.W.; Yang, Z.D.; Gao, X.W.; Liu, H. Hetero-structure La₂O₃-modified SnO₂-Sn₃O₄ from tin anode slime for highly sensitive and ppb-Level formaldehyde detection. *Appl. Surf. Sci.* **2020**, *513*, 145825. [[CrossRef](#)]
6. Xu, L.; Ge, M.Y.; Zhang, F.; Huang, H.J.; Sun, Y.; He, D.N. Nanostructured of SnO₂/NiO composite as a highly selective formaldehyde gas sensor. *J. Mater. Res.* **2020**, *35*, 3079–3090. [[CrossRef](#)]
7. Liu, Z.; Sun, D.D.; Guo, P.; Leckie, J.O. An Efficient Bicomponent TiO₂/SnO₂ Nanofiber Photocatalyst Fabricated by Electrospinning with a Side-by-Side Dual Spinneret Method. *Nano Lett.* **2007**, *7*, 1081–1085. [[CrossRef](#)]
8. Tennakone, K.; Bandara, J.; Bandaranayake, P.K.M.; Kumara, G.R.A.; Konno, A. Enhanced Efficiency of a Dye-Sensitized Solar Cell Made from MgO-Coated Nanocrystalline SnO₂. *Jpn. J. Appl. Phys.* **2001**, *40*, 732. [[CrossRef](#)]
9. Liu, J.; Dai, M.; Wang, T.; Sun, P.; Liang, X.; Lu, G.; Shimano, K.; Yamazoe, N. Enhanced Gas Sensing Properties of SnO₂ Hollow Spheres Decorated with CeO₂ Nanoparticles Heterostructure Composite Materials. *ACS Appl. Mater. Interfaces* **2016**, *8*, 6669–6677. [[CrossRef](#)] [[PubMed](#)]
10. Jiang, J.; Shi, L.; Xie, T.; Wang, D.; Lin, Y. Study on the Gas-Sensitive Properties for Formaldehyde Based on SnO₂-ZnO Heterostructure in UV Excitation. *Sens. Actuators B Chem.* **2018**, *254*, 863–871. [[CrossRef](#)]
11. Huang, H.; Gong, H.; Chow, C.L.; Guo, J.; White, T.J.; Tse, M.S.; Tan, O.K. Low-Temperature Growth of SnO₂ Nanorod Arrays and Tunable n-p-n Sensing Response of a ZnO/SnO₂ Heterojunction for Exclusive Hydrogen Sensors. *Adv. Funct. Mater.* **2011**, *21*, 2680–2686. [[CrossRef](#)]
12. Liu, D.; Tang, Z.L.; Zhang, Z.T. Visible Light Assisted Room-Temperature NO₂ Gas Sensor Based on Hollow SnO₂@SnS₂ Nanostructures. *Sens. Actuators B Chem.* **2020**, *324*, 128754. [[CrossRef](#)]
13. Ju, D.; Xu, H.; Xu, Q.; Gong, H.; Qiu, Z.; Guo, J.; Zhang, J.; Cao, B. High Triethylamine-Sensing Properties of NiO/SnO₂ Hollow Sphere P-N Heterojunction Sensors. *Sens. Actuators B Chem.* **2015**, *215*, 39–44. [[CrossRef](#)]
14. Kim, J.-H.; Lee, J.-H.; Mirzaei, A.; Kim, H.W.; Kim, S.S. Optimization and Gas Sensing Mechanism of n-SnO₂-p-Co₃O₄ Composite Nanofibers. *Sens. Actuators B Chem.* **2017**, *248*, 500–511. [[CrossRef](#)]
15. Zhang, B.W.; Fu, W.Y.; Li, H.Y.; Fu, X.L.; Wang, Y.; Bala, H.; Sun, G.; Wang, X.D.; Wang, Y.; Cao, J.L.; et al. Actinomorphic ZnO/SnO₂ Core-Shell Nanorods: Two-Step Synthesis and Enhanced Ethanol Sensing Properties. *Mater. Lett.* **2015**, *160*, 227–230. [[CrossRef](#)]
16. Chen, K.; Chen, S.; Pi, M.; Zhang, D. SnO₂ Nanoparticles/TiO₂ Nanofibers Heterostructures: In Situ Fabrication and Enhanced Gas Sensing Performance. *Solid State Electron.* **2019**, *157*, 42–47. [[CrossRef](#)]
17. Sardar, K.; Fang, T.; Yang, T.W. A novel route involving an in situ chemical reduction process to the one-dimensional nanostructures of bismuth trioxide. *J. Am. Ceram. Soc.* **2007**, *90*, 4033–4035. [[CrossRef](#)]
18. Bonyani, M.; Lee, J.K.; Sun, G.-J.; Lee, S.; Ko, T.; Lee, C. Benzene sensing properties and sensing mechanism of Pd-decorated Bi₂O₃-core/ZnO-shell nanorods. *Thin Solid Films* **2017**, *636*, 257–266. [[CrossRef](#)]
19. Chen, Q.; Tan, X.; Dastan, D.; Zhang, Z.; Liu, Z.; Yue, C.; Yang, Z.; Mu, Y.; Wang, X.; Chen, X.; et al. Ultrasensitive n-butanol gas sensor based on Bi₂O₃-In₂O₃ heterostructure. *J. Alloys Compd.* **2024**, *1003*, 175585. [[CrossRef](#)]
20. Meng, X.; Kang, S.; Zhao, Z.; Jin, G.; Shao, Z.; Wu, L. Core-Shell Bi₂O₃/CeO₂ heterojunction for enhanced formaldehyde gas sensor. *Ceram. Int.* **2024**. [[CrossRef](#)]
21. Devi, G.S.; Manorama, S.V.; Rao, V.J. SnO₂/Bi₂O₃: A Suitable System for Selective Carbon Monoxide Detection. *J. Electrochem. Soc.* **1998**, *145*, 1039–1044. [[CrossRef](#)]
22. Montenegro, A.; Ponce, M.; Castro, M.S.; Rodríguez-Paez, J.E. SnO₂-Bi₂O₃ and SnO₂-Sb₂O₃ Gas Sensors Obtained by Soft Chemical Method. *J. Eur. Ceram. Soc.* **2007**, *27*, 4143–4146. [[CrossRef](#)]
23. Bang, J.H.; Choi, M.S.; Mirzaei, A.; Kwon, Y.J.; Kim, S.S.; Kim, T.W.; Kim, H.W. Selective NO₂ Sensor Based on Bi₂O₃ Branched SnO₂ Nanowires. *Sens. Actuators B Chem.* **2018**, *274*, 356–369. [[CrossRef](#)]
24. Yang, H.; Suematsu, K.; Mashiba, F.H.; Watanabe, K.; Shimano, K. Oxygenated VOC Detection Using SnO₂ Nanoparticles with Uniformly Dispersed Bi₂O₃. *Nanomaterials* **2024**, *14*, 2032. [[CrossRef](#)] [[PubMed](#)]
25. Sun, L.; Sun, J.; Han, N.; Liao, D.; Bai, S.; Yang, X. rGO decorated W doped BiVO₄ novel material for sensing detection of trimethylamine. *Sens. Actuators B* **2019**, *298*, 126749. [[CrossRef](#)]
26. Yu, C.F.; Wang, K.; Yang, P.Y.; Yang, S.N.; Lu, C.; Song, Y.Z.; Dong, S.Y.; Sun, J.Y.; Sun, J.H. One-pot facile synthesis of Bi₂S₃/SnS₂/Bi₂O₃ ternary heterojunction as advanced double Z-scheme photocatalytic system for efficient dye removal under sunlight irradiation. *Appl. Surf. Sci.* **2017**, *420*, 233–242. [[CrossRef](#)]
27. Bai, J.Z.; Shen, Y.B.; Zhao, S.K.; Li, A.; Kang, Z.K.; Cui, B.Y.; Wei, D.Z.; Yuan, Z.Y.; Meng, F.L. Room-Temperature NH₃ Sensor Based on SnO₂ Quantum Dots Functionalized SnS₂ Nanosheets. *Adv. Mater. Technol.* **2023**, *8*, 2201671. [[CrossRef](#)]

28. Kou, X.Y.; Meng, F.Q.; Chen, K.; Wang, T.S.; Sun, P.; Liu, F.M.; Yan, X.; Sun, Y.F.; Liu, F.M.; Shimano, K.; et al. High-performance acetone gas sensor based on Ru-doped SnO₂ nanofibers. *Sens. Actuators B* **2020**, *320*, 128292. [[CrossRef](#)]
29. Liu, H.; Du, C.; Li, M.; Zhang, S.; Bai, H.; Yang, L.; Zhang, S. One-Pot Hydrothermal Synthesis of SnO₂/BiOBr Heterojunction Photocatalysts for the Efficient Degradation of Organic Pollutants Under Visible Light. *ACS Appl. Mater. Interfaces* **2018**, *10*, 28686–28694. [[CrossRef](#)]
30. Meng, X.; Bi, M.; Gao, W. Shape and composition effects of PdPt bimetallic nanocrystals on hydrogen sensing properties of SnO₂ based sensors. *Sens. Actuators B* **2023**, *390*, 133976. [[CrossRef](#)]
31. Kaneti, Y.V.; Zhang, Z.; Yue, J.; Zakaria, Q.M.D.; Chen, C.; Jiang, X.; Yu, A. Crystal plane-dependent gas-sensing properties of zinc oxide nanostructures: Experimental and theoretical studies. *Phys. Chem. Chem. Phys.* **2014**, *16*, 11471–11480. [[CrossRef](#)] [[PubMed](#)]
32. Bhattacharyya, P.; Basu, P.K.; Mondal, B.; Saha, H. A low power MEMS gas sensor based on nanocrystalline ZnO thin films for sensing methane. *Microelectron. Reliab.* **2008**, *48*, 1772–1779. [[CrossRef](#)]
33. Massie, C.; Stewart, G.; McGregor, G.; Gilchrist, J.R. Design of a portable optical sensor for methane gas detection. *Sens. Actuators B Chem.* **2006**, *113*, 830–836. [[CrossRef](#)]
34. Han, Z.J.; Qi, Y.; Yang, Z.Y.; Han, H.C.; Jiang, Y.Y.; Du, W.J.; Zhang, X.; Zhang, J.Z.; Dai, Z.F.; Wu, L.L.; et al. Recent advances and perspectives on constructing metal oxide semiconductor gas sensing materials for efficient formaldehyde detection. *J. Mater. Chem. C* **2020**, *8*, 13169–13188. [[CrossRef](#)]
35. Shaalan, N.M.; Rashad, M.; Abdel-Rahim, M.A. Repeatability of indium oxide gas sensors for detecting methane at low temperature. *Mater. Sci. Semicond. Process.* **2016**, *56*, 260–264. [[CrossRef](#)]
36. Lee, D.-D.; Chung, W.-Y.; Sohn, B.-K. High sensitivity and selectivity methane gas sensors doped with Rh as a catalyst. *Sens. Actuators B Chem.* **1993**, *13*, 252–255. [[CrossRef](#)]
37. Haridas, D.; Gupta, V. Enhanced response characteristics of SnO₂ thin film based sensors loaded with Pd clusters for methane detection. *Sens. Actuators B Chem.* **2012**, *166–167*, 156–164. [[CrossRef](#)]
38. Shaalan, N.M.; Hamad, D. Low-temperature hydrogen sensor based on sputtered tin dioxide nanostructures through slow deposition rate. *Appl. Surf. Sci.* **2022**, *598*, 153857. [[CrossRef](#)]
39. Liu, M.; Sun, R.Y.; Sima, Z.H.; Song, P.; Ding, Y.L.; Wang, Q. Au-decorated In₂O₃ nanospheres/exfoliated Ti₃C₂T_x MXene nanosheets for highly sensitive formaldehyde gas sensing at room temperature. *Appl. Surf. Sci.* **2022**, *605*, 154839. [[CrossRef](#)]
40. Meng, D.; Liu, D.; Wang, G.; Shen, Y.; San, X.; Li, M.; Meng, F. Low-temperature formaldehyde gas sensors based on NiO-SnO₂ heterojunction microflowers assembled by thin porous nanosheets. *Sens. Actuators B Chem.* **2018**, *273*, 418–428. [[CrossRef](#)]
41. Chowdhuri, A.; Gupta, V.; Sreenivas, K.; Kumar, R.; Mozumdar, S.; Patanjali, P.K. Response speed of SnO₂-based H₂S gas sensors with CuO nanoparticles. *Appl. Phys. Lett.* **2004**, *84*, 1180–1182. [[CrossRef](#)]
42. Xue, X.; Xing, L.; Chen, Y.; Shi, S.; Wang, Y.; Wang, T. Synthesis and H₂S sensing properties of CuO–SnO₂ core/shell pn-junction nanorods. *J. Phys. Chem. C* **2008**, *112*, 12157–12160. [[CrossRef](#)]
43. Zhao, Y.; Zhang, J.; Wang, Y.; Chen, Z. A Highly Sensitive and Room Temperature CNTs/SnO₂/CuO Sensor for H₂S Gas Sensing Applications. *Nanoscale Res. Lett.* **2020**, *15*, 40. [[CrossRef](#)] [[PubMed](#)]
44. Liu, Y.; Xiao, S.; Du, K. Chemiresistive Gas Sensors Based on Hollow Heterojunction: A Review. *Adv. Mater. Interfaces* **2021**, *8*, 2002122. [[CrossRef](#)]
45. Tyagi, P.; Sharma, A.; Tomar, M.; Gupta, V. A comparative study of RGO-SnO₂ and MWCNT-SnO₂ nanocomposites based SO₂ gas sensors. *Sens. Actuators B Chem.* **2017**, *248*, 980–986. [[CrossRef](#)]

Disclaimer/Publisher’s Note: The statements, opinions and data contained in all publications are solely those of the individual author(s) and contributor(s) and not of MDPI and/or the editor(s). MDPI and/or the editor(s) disclaim responsibility for any injury to people or property resulting from any ideas, methods, instructions or products referred to in the content.